J Eng Math (2008) 60:127–147
DOI 10.1007/s10665-006-9134-2

Two-layer flow in a corrugated channel

H. Luo · M. G. Blyth · C. Pozrikidis

Received: 13 January 2006 / Accepted: 13 December 2006 / Published online: 14 April 2007

Abstract The flow of two superposed viscous fluid layers in a two-dimensional channel confined between a plane and a wavy or indented wall is studied by analytical and numerical methods at arbitrary Reynolds numbers. The interface between the two fluids may exhibit constant or variable surface tension due to an insoluble surfactant. The flow is computed from a specified initial condition using the immersed-interface method on a curvilinear grid constructed by conformal mapping. The numerical simulations illustrate the effect of geometrical nonlinearity and reveal that inertia may increase or decrease the amplitude of the interface profile at steady state depending on the flow parameters. Increasing either the Reynolds number or the wall amplitude above a certain threshold value provokes flow instability and overturning of the interface. In the Appendix, a linear perturbation analysis is performed for arbitrary Reynolds numbers on the assumption of small-amplitude sinusoidal undulations, and results for the amplitude and phase shift of the interfacial and surfactant concentration wave are documented for a broad range of flow conditions. It is found that inertia may have a mixed effect on the deformation and phase shift, while the surfactant promotes the deformation of the interface under most conditions.

Keywords Channel flow · Immersed-interface method · Marangoni instability · Surfactants

1 Introduction

Flow over a wall with isolated or distributed surface roughness is an important topic of fundamental and applied research. The effect of wall roughness has been addressed by a number of workers for homogeneous channel flow in the context of tribology and with the intention of further explaining the process of laminar–turbulent transition

H. Luo
Department of Mechanical and Aerospace Engineering, George Washington University, Suite T739, 801 22nd St. NW
Washington, DC 20052 USA
e-mail: hluo@gwu.edu

M. G. Blyth (✉)
School of Mathematics, University of East Anglia, Norwich, England NR4 7TJ, UK
e-mail: m.blyth@uea.ac.uk

C. Pozrikidis
Department of Mechanical and Aerospace Engineering, University of California, San Diego, La Jolla, CA 92093-0411 USA
e-mail: cpozrikidis@ucsd.edu

(see, e.g., [1,2]). When two or more fluid layers are present, attention is focused upon the shape and various modes of instability of the interfaces. From a practical standpoint, the flow of a liquid film or multi-layered system arises in a broad range of important industrial applications including the manufacture of electronic components, the fabrication of active glass screens, and photographic coating technology. The underlying surface may be corrugated deliberately in order to produce patterning effects, or else the surface roughness may be a natural but undesirable feature creating unwanted distortion.

A number of authors have studied steady two-dimensional film flow down a corrugated wall. Wang [3] conducted an asymptotic analysis based on small-amplitude wall roughness. Kang and Chen [4] looked at two-layer flow down a wavy wall for small Reynolds numbers. Experiments performed by Vlachogiannis and Bontozoglou [6] revealed that steady free-surface profiles can be realised, even for quite large Reynolds numbers on the order of a hundred. The profiles have the same wavelength as the wall indentations, but the amplitude and phase depends on the Reynolds number. Wierschem et al. [7] conducted further experiments and paid particular attention to the vortices generated in the troughs at small Reynolds numbers.

In the current work, we consider two-layer steady flow in a two-dimensional channel confined between a planar upper wall and an uneven lower wall. In a companion paper, Luo and Pozrikidis [8] examined the flow in the limit of vanishing Reynolds number and accounted for the effect of an insoluble surfactant. The main objective was to describe the significance of the wall corrugations on the shape of the interface and assess the effect of the surfactant at steady state. Consideration of the surfactant was partly motivated by the recent discovery that the Marangoni traction due to variations in the surfactant concentration promotes the deformation of the free surface of a liquid film down an inclined corrugated wall in Stokes flow [5].

Luo and Pozrikidis [8] performed a perturbation analysis for a channel wall with small-amplitude sinusoidal corrugations, and confirmed that the surfactant amplifies the deformation of the interface and causes a negative drift in the phase shift under most conditions. The effect was shown to be most significant at moderate capillary numbers and for wall corrugations whose wave length is large compared to the thickness of the adjacent layer lining the wavy wall. Parametric investigations revealed that the precise effect of the surfactant depends on the ratio of the fluid viscosities, proximity of the interface to the planar wall, capillary number, and wave length of the corrugations. When the interface is near the plane wall, introducing surfactant reduces the interfacial amplitude and causes a positive phase shift with respect to the wavy wall in shear-driven flow. As the interface further approaches the plane wall, the interfacial wave tends to become in phase with the wavy wall, reflecting its unshifted topography. Luo and Pozrikidis [8] further implemented a boundary-integral method to compute Stokes flow over a wall with a periodic profile, and presented results for sinusoidal walls and planar walls containing a periodic sequence of square and circular depressions or projections. The boundary-integral computations revealed that the linear perturbation theory overestimates the deformation of the interface and illustrated the nature of shear-driven film flow over a planar wall with indented topography.

In this paper, the previous analysis is extended into the regime of inertial flow with the goal of describing the effect of the Reynolds number. A numerical method is developed for computing flow in a periodic channel with arbitrary geometry using the immersed-interface formulation in curvilinear coordinates by conformal mapping. In addition, a linearised analysis is performed in the context of only minor wall roughness and the results are shown to be consistent with the nonlinear calculations. Parametric investigations for a variety of wall geometries illustrate the effect of inertial and geometrical nonlinearity for significantly uneven profiles.

2 Problem statement

We consider two-dimensional flow of two superposed liquid layers in a horizontal channel confined by a planar upper wall and a periodic lower wall with wave length L, as illustrated in Fig. 1a. The lower and upper layers are labeled as 1 and 2, respectively. The fluid motion is driven either by the translation of the upper wall parallel to itself with velocity U (shear-driven flow), or by an imposed streamwise pressure gradient (pressure-driven flow).

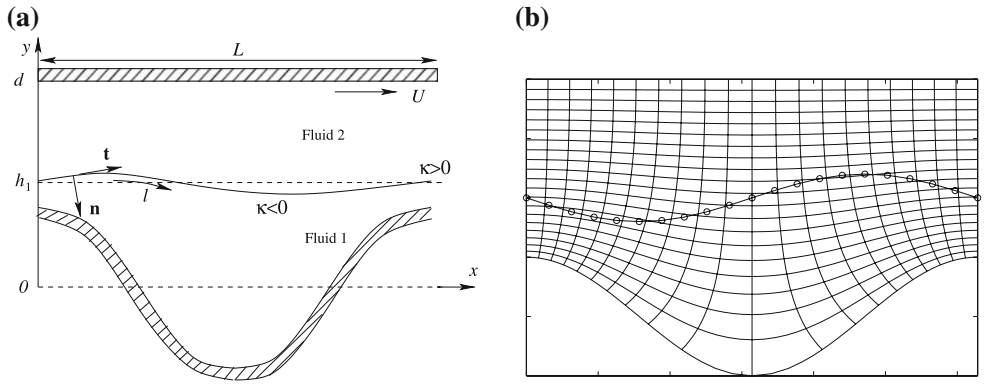

Fig. 1 (**a**) Schematic illustration of two-layer flow in a channel confined by a planar upper wall and a corrugated lower wall. (**b**) Orthogonal curvilinear grid produced by conformal mapping for solving the Navier–Stokes equation, and distribution of the interfacial marker points

The flow in each layer is governed by the Navier–Stokes equation,

$$\rho_j \left(\frac{\partial \mathbf{u}}{\partial t} + \mathbf{u} \cdot \nabla \mathbf{u} \right) = -\nabla p + \mu_j \nabla^2 \mathbf{u}, \qquad \nabla \cdot \mathbf{u} = 0, \tag{2.1}$$

where $\mathbf{u} = (u_x, u_y)$ is the velocity, p is the pressure, μ_j are the fluid viscosities, ρ_j are the fluid densities, and $j = 1, 2$ correspond to the lower and upper fluid, respectively. The upper wall is located at $y = d$, and the lower wall is described by the periodic function $y = y_w(x)$. In the remainder of this paper, we consider neutrally buoyant fluids, and set $\rho_1 = \rho_2 = \rho$.

The velocity is required to satisfy the no-slip and no-penetration conditions at the lower and the upper walls and to vary continuously across the interface. The hydrodynamic traction undergoes a discontinuity given by

$$\Delta \mathbf{f} \equiv (\boldsymbol{\sigma}^{(1)} - \boldsymbol{\sigma}^{(2)}) \cdot \mathbf{n} = -\frac{\partial(\gamma \mathbf{t})}{\partial l} = -\gamma \kappa \mathbf{n} - \frac{\partial \gamma}{\partial l} \mathbf{t}, \tag{2.2}$$

where $\boldsymbol{\sigma}^{(j)}$ is the Newtonian stress tensor in the jth fluid on either side of the interface, γ is the position-dependent surface tension, $\mathbf{n}$ is the unit normal vector pointing into the lower fluid, $\mathbf{t}$ is the unit tangent vector pointing in the direction of increasing arc length l, and $\kappa = \mathbf{n} \cdot \mathrm{d}\mathbf{t}/\mathrm{d}l$ is the curvature of the interface in the xy plane, reckoned to be positive when the interface is downward parabolic, as illustrated in Fig. 1a.

The interface is populated with an insoluble surfactant that is convected and diffuses along the interface according to the transport equation

$$\frac{\mathrm{d}\Gamma}{\mathrm{d}t} + \frac{\partial(u_t \Gamma)}{\partial l} = -\Gamma \kappa u_n + D_s \frac{\partial^2 \Gamma}{\partial l^2}, \tag{2.3}$$

where $u_t = \mathbf{u} \cdot \mathbf{t}$ is the tangential velocity, $u_n = -\mathbf{u} \cdot \mathbf{n}$ is the normal velocity, and D_s is the surfactant diffusivity (e.g., [9,10]). The derivative $\mathrm{d}/\mathrm{d}t$ on the left-hand side of (2.3) expresses the rate of change of a variable following an interfacial marker point moving with the local fluid velocity normal to the interface. When the surfactant concentration is well below the saturation level, a linear relationship may be assumed between the surface tension and the surfactant concentration according to Gibbs' law, $\gamma_c - \gamma = \Gamma E$, where E is the surface elasticity and γ_c is the surface tension of a clean interface devoid of surfactants (e.g., [11,12]). In terms of the dimensionless physiochemical parameter $\beta = \Gamma_0 E/\gamma_c$, the linear equation of state reads

$$\gamma = \frac{\gamma_0}{1-\beta} \left(1 - \beta \frac{\Gamma}{\Gamma_0} \right), \tag{2.4}$$

where Γ_0 is a reference concentration corresponding to the surface tension $\gamma_0 = \gamma_c (1-\beta)$. The significance of the surfactant is expressed by the dimensionless Marangoni number,

$$\mathrm{Ma} \equiv \frac{E\Gamma_0}{\gamma_0} = \frac{\beta}{1-\beta}. \tag{2.5}$$

Given an initial condition, the dynamics of the flow depends on the ratio of the fluid volumes contained within each period, r, viscosity ratio, $\lambda \equiv \mu_2/\mu_1$, Marangoni number, Ma, and reduced lower-wall profile $\hat{y}_w \equiv y_w/d$. In the case of shear-driven flow, the dynamics also depends on the capillary and Reynolds numbers

$$\mathrm{Ca}_S = \frac{\mu_1 U}{\gamma_0}, \quad \mathrm{Re}_S = \frac{\rho\, U d}{\mu_1}. \tag{2.6}$$

In the case of pressure-driven flow, the capillary and Reynolds numbers are defined as

$$\mathrm{Ca}_P = \frac{\chi d^2}{\gamma_0}, \quad \mathrm{Re}_P = \frac{\rho\, \chi d^3}{\mu_1^2}, \tag{2.7}$$

where χ is the negative of the mean streamwise pressure gradient.

3 Numerical simulations for arbitrary wall amplitude

To study flow in a channel with an arbitrary profile, we solve the Navier–Stokes equation (2.1) subject to the no-slip and no-penetration conditions over each wall, and the stress balance expressed by (2.2) along the interface. The numerical procedure is based on Peskin's immersed-interface formulation (e.g. [13]) combined with a finite-difference method implemented in orthogonal curvilinear coordinates constructed by conformal mapping. A similar method was implemented by Pozrikidis [14] on a Cartesian grid for two-layer flow in a channel confined by two plane parallel walls, and by Blyth et al. [15] for computing axisymmetric waves in core-annular flow. The novelty of the present method lies in the implementation of the immersed-interface formulation in curvilinear coordinates.

3.1 Conformal mapping

Consider a periodic flow cell, as illustrated in Fig. 1b. To implement the finite-difference method, we introduce a conformal mapping that maps the depicted flow cell into the rectangular region $0 \le \xi \le 2\pi$, $0 \le \eta \le \eta_T$ in the $\xi\eta$ parameter space,

$$(x, y) = \mathcal{F}(\xi, \eta), \tag{3.1}$$

expressed by

$$\begin{aligned} \frac{x}{L/2\pi} &= \xi + \sum_{n=1}^{\infty} \frac{b_n}{n} \sin(n\xi) \left\{ \frac{\cosh[n(\eta_T - \eta)]}{\sinh(n\,\eta_T)} \right\}, \\ \frac{y}{L/2\pi} &= \eta + b_0 - \sum_{n=1}^{\infty} \frac{b_n}{n} \cos(n\xi) \left\{ \frac{\sinh[n(\eta_T - \eta)]}{\sinh(n\,\eta_T)} \right\}, \end{aligned} \tag{3.2}$$

where b_n are a priori unknown constant coefficients, and $\eta_T = 2\pi d/L - b_0$ [16]. In the practical implementation, the infinite series on the right-hand side of (3.2) are truncated after N_b terms. To compute the unknown constants, b_n, we distribute N_p evenly spaced points along the line $\eta = 0$, for $0 \le \xi \le 2\pi$, and require that their images lie on the prescribed lower wall in the xy-plane. The coefficients, b_n, are then computed by minimizing the approximation error in a least-squares sense using a gradient-based optimization method. For flow over a sinusoidal wall discussed later in this section, we have used $N_b \le 30$ and $N_p = 200$. Once the mapping coefficients are available, the mapping of a point from the parameter space to the physical space arises explicitly from (3.2). To compute the inverse mapping of a point from the physical space to a point in the parameter space, we solve the nonlinear equation (3.2)

using Newton's method. Typically, only a few iterations are required to achieve convergence to within a specified tolerance. The Jacobian matrix of the transformation is given by

$$\mathbf{J} \equiv \begin{bmatrix} \cos\theta & -\sin\theta \\ \sin\theta & \cos\theta \end{bmatrix} = \frac{1}{\mathcal{J}} \begin{bmatrix} \frac{\partial x}{\partial \xi} & \frac{\partial x}{\partial \eta} \\ \frac{\partial y}{\partial \xi} & \frac{\partial y}{\partial \eta} \end{bmatrix}, \qquad \mathcal{J} \equiv \sqrt{\left(\frac{\partial x}{\partial \xi}\right)^2 + \left(\frac{\partial x}{\partial \eta}\right)^2}, \tag{3.3}$$

where θ is the local clockwise rotation angle at the intersection of the curvilinear and Cartesian coordinates.

3.2 Governing equations and numerical method

In the numerical implementation, the discontinuous viscosity field is replaced by a smooth distribution expressed in terms of a mollifying function $c(\xi, \eta)$ which takes the value of zero in the bulk of the lower fluid, the value of unity in the bulk of the upper fluid, and undergoes a rapid transition across the interface, $\mu(\xi, \eta) = \mu_1 + (\mu_2 - \mu_1)\, c(\xi, \eta)$ (e.g., [14,15]). The mollifying function in the $\xi\eta$-plane is computed on the basis of the following integral representation for the gradient

$$\hat{\nabla} c(\xi, \eta) = -\mathbf{J}^{-1}(\mathbf{x}) \cdot \int_I \mathcal{D}_2(\mathbf{x} - \mathbf{x}')\, \mathbf{n}(\mathbf{x}')\, \mathrm{d}l(\mathbf{x}'), \tag{3.4}$$

where $\hat{\nabla} = (1/\mathcal{J})\ [\partial/\partial\xi, \quad \partial/\partial\eta]$, $\mathcal{D}_2$ is Dirac's delta function in the xy-plane with dimension of inverse squared length, and l is the arc length along the interface I. The integral on the right-hand side of (3.4) is evaluated at the nodes of a finite-difference grid in the xy-space and then mapped onto the corresponding grid nodes in the $\xi\eta$-plane. The delta function inside the integral is approximated with a smooth but narrowly distributed function, as will be discussed later in this section. Taking the divergence of (3.4) written for the smoothed delta function, we derive a Poisson equation for $c(\xi, \eta)$, which is solved subject to the periodic boundary condition in the ξ direction, and the Dirichlet boundary conditions $c = 0$ at $\eta = 0$ and $c = 1$ at $\eta = \eta_T$.

Next, we express the velocity in terms of its components in the orthogonal curvilinear coordinates, $\hat{\mathbf{u}} = (u_\xi, u_\eta)$, and introduce a generalized Navier–Stokes equation incorporating the jump in viscosity and traction at the interface

$$\rho \left(\frac{\partial \hat{\mathbf{u}}}{\partial t} + \hat{\mathbf{u}} \cdot \hat{\nabla} \hat{\mathbf{u}} \right) = -\hat{\nabla} p + 2\, \hat{\nabla} \cdot (\mu \hat{\mathbf{E}}) + \hat{\mathbf{B}}, \tag{3.5}$$

where $\hat{\mathbf{E}} = (1/2)\ (\hat{\nabla}\hat{\mathbf{u}} + \hat{\nabla}\hat{\mathbf{u}}^T)$ is the rate-of-deformation tensor, $\hat{\mathbf{B}}$ is the body force vector accounting for the jump in the interfacial traction,

$$\hat{\mathbf{B}} = \hat{\mathbf{B}}(\mathcal{F}^{-1}(\mathbf{x})) = -\mathbf{J}^{-1}(\mathbf{x}) \cdot \int_I \mathcal{D}_2(\mathbf{x} - \mathbf{x}')\, \Delta\mathbf{f}(\mathbf{x}')\, \mathrm{d}l(\mathbf{x}'), \tag{3.6}$$

and $\Delta\mathbf{f}$ is the jump in the interfacial traction defined in (2.2). The orthogonal curvilinear components of the divergence of the deviatoric part of the stress tensor can be expressed in the form

$$2\hat{\nabla} \cdot (\mu\, \hat{\mathbf{E}}) = \mu \hat{\nabla}^2 \hat{\mathbf{u}} + \hat{\nabla}\mu \times \hat{\boldsymbol{\omega}} + 2\, \hat{\nabla}\mu \cdot \hat{\nabla}\hat{\mathbf{u}}, \tag{3.7}$$

where $\hat{\boldsymbol{\omega}} \equiv \hat{\nabla} \times \hat{\mathbf{u}}$ is the vorticity. The second and third terms on the right-hand side of (3.7) are non-zero only along the interface. Because $\hat{\nabla}\mu$ is normal to the interface, the second term makes a contribution that is tangential to the interface.

One period of the interface is traced with N_I interfacial nodes in the physical space, $\mathbf{x}_k$, $k = 1, 2, \ldots, N_I$, and the interfacial profile, $(x(s), y(s))$, is reconstructed from the nodal positions using periodic cubic-spline interpolation in physical space, as shown in Fig. 1b. At the nodes, the interpolation parameter, s, is identified with the current length of a polygonal line connecting adjacent nodes, measured from the first node. Once the shape of the interface has been constructed, the normal and tangential vectors, $\mathbf{n}$ and $\mathbf{t}$, are computed using standard formulae from differential geometry, and the curvature of the interface in the xy space is calculated using the formula

$$\kappa = \frac{x''y' - y''x'}{(x'^2 + y'^2)^{3/2}}, \tag{3.8}$$

where a prime denotes a derivative with respect to the interpolation parameter, s. At each time step, the nodes are adaptively redistributed to ensure adequate spatial resolution and prevent clustering [14]. The surfactant concentration at the new nodes is obtained by polynomial interpolation.

In the immersed-interface method inspired by Peskin's immersed-boundary method, the singular delta function $\mathcal{D}_2(\mathbf{x})$ associated with each node is replaced by a smooth function that is supported by a rectangular region centered at the node. For the kth node, we use the approximation

$$\mathcal{D}_2(\mathbf{x}-\mathbf{x}_k) \simeq \mathcal{H}_2(\mathbf{x}-\mathbf{x}_k) \equiv \frac{1}{16\,\delta_1\delta_2}\,(1+\cos\hat{x})(1+\cos\hat{y}) \tag{3.9}$$

for $|x-x_k| < 2\delta_1$ and $|y-y_k| < 2\delta_2$, where $\hat{x} \equiv \pi(x-x_k)/(2\,\delta_1)$, $\hat{y} \equiv \pi(y-y_k)/(2\,\delta_2)$, $\delta_1 \equiv (\Delta x)^q$, $\delta_2 \equiv (\Delta y)^q$, $\Delta x \equiv L/N_\xi$ and $\Delta y \equiv d/N_\eta$ are averaged spatial discretization intervals in the physical space, N_ξ and N_η are the spatial resolutions of the finite-difference grid in the ξ and η directions, and q is a numerical parameter controlling the spreading length of the delta function. Applying the trapezoidal rule to evaluate the line integral on the right-hand side of (3.6), we find

$$\int_I \mathcal{D}_2(\mathbf{x}-\mathbf{x}')\,\Delta\mathbf{f}(\mathbf{x}')\,\mathrm{d}l(\mathbf{x}') \simeq \sum_{k=1}^{N_I} \mathcal{H}_2(\mathbf{x}-\mathbf{x}_k)\,\Delta\mathbf{f}_k\,\frac{l_{k+1}-l_{k-1}}{2}, \tag{3.10}$$

where l_k is the arc length measured from the reference point to the kth node. The jump in the interfacial traction at the kth node, $\Delta\mathbf{f}_k$, is evaluated using the finite-difference approximation

$$\Delta\mathbf{f}_k = -\left(\frac{\mathbf{x}_{k+1}-\mathbf{x}_k}{|\mathbf{x}_{k+1}-\mathbf{x}_k|}\,\frac{\gamma_{k+1}+\gamma_k}{2} - \frac{\mathbf{x}_k-\mathbf{x}_{k-1}}{|\mathbf{x}_k-\mathbf{x}_{k-1}|}\,\frac{\gamma_k+\gamma_{k-1}}{2}\right)\frac{2}{l_{k+1}-l_{k-1}} \tag{3.11}$$

based on the middle expression in (2.2).

To compute the evolution of the flow from a specified initial condition, we use a variation of Chorin's projection method. The algorithm involves a series of elementary sub-steps based on the constituent evolution equations

$$\begin{gathered}
\rho\,\frac{\partial\hat{\mathbf{u}}}{\partial t} = -\chi\,\hat{\mathbf{e}} + \hat{\nabla}\mu\times\hat{\boldsymbol{\omega}} + \hat{\mathbf{B}} - \rho\,\hat{\mathbf{v}}\cdot\begin{bmatrix} \frac{u_\eta}{\mathcal{J}^2}\frac{\partial\mathcal{J}}{\partial\eta} & -\frac{u_\eta}{\mathcal{J}^2}\frac{\partial\mathcal{J}}{\partial\xi} \\ -\frac{u_\xi}{\mathcal{J}^2}\frac{\partial\mathcal{J}}{\partial\eta} & \frac{u_\xi}{\mathcal{J}^2}\frac{\partial\mathcal{J}}{\partial\xi} \end{bmatrix}, \\
\rho\left(\frac{\partial\hat{\mathbf{u}}}{\partial t} + \hat{\mathbf{v}}\cdot\hat{\nabla}^{(1)}\hat{\mathbf{u}}\right) = \mu\,\hat{\nabla}^2\hat{\mathbf{u}}, \qquad \rho\,\frac{\partial\hat{\mathbf{u}}}{\partial t} = -\hat{\nabla}\phi,
\end{gathered} \tag{3.12}$$

where χ is a specified constant pressure gradient, $\hat{\mathbf{e}} = \mathbf{J}^{-1}\cdot\mathbf{e}_x$, $\mathbf{e}_x$ is the unit vector along the x-axis in the xy-plane, ϕ is a projection function regarded as an approximation of the non-periodic part of the pressure (e.g., [17,18]), and

$$\hat{\mathbf{v}} \equiv \hat{\mathbf{u}} - \frac{2}{\rho}\,\hat{\nabla}\mu, \quad \hat{\nabla}^{(1)}\hat{\mathbf{u}} \equiv \begin{bmatrix} \frac{1}{\mathcal{J}}\frac{\partial u_\xi}{\partial\xi} & \frac{1}{\mathcal{J}}\frac{\partial u_\xi}{\partial\eta} \\ \frac{1}{\mathcal{J}}\frac{\partial u_\eta}{\partial\xi} & \frac{1}{\mathcal{J}}\frac{\partial u_\eta}{\partial\eta} \end{bmatrix}. \tag{3.13}$$

To expedite the simulations, the second step in (3.12) is further decomposed into two one-dimensional convection–diffusion steps,

$$\begin{gathered}
\rho\left(\frac{\partial\hat{\mathbf{u}}}{\partial t} + v_\xi\,\frac{1}{\mathcal{J}}\frac{\partial\hat{\mathbf{u}}}{\partial\xi}\right) = \mu\mathcal{L}^{(1)}(\hat{\mathbf{u}}), \\
\rho\left(\frac{\partial\hat{\mathbf{u}}}{\partial t} + v_\eta\,\frac{1}{\mathcal{J}}\frac{\partial\hat{\mathbf{u}}}{\partial\eta}\right) = \mu\mathcal{L}^{(2)}(\hat{\mathbf{u}}) + \mu\,\mathcal{L}^{(3)}(\hat{\mathbf{u}}),
\end{gathered} \tag{3.14}$$

where $\mathcal{L}^{(i)}(\hat{\mathbf{u}})$, $i = 1, 2, 3$, are individual splittings of $\hat{\nabla}^2\hat{\mathbf{u}}$, given by

$$\mathcal{L}^{(1)}(\hat{\mathbf{u}}) \equiv \frac{1}{\mathcal{J}^2}\left[\frac{\partial^2\hat{\mathbf{u}}}{\partial\xi^2} - \frac{\hat{\mathbf{u}}}{\mathcal{J}}\left(\frac{\partial^2\mathcal{J}}{\partial\xi^2} + \frac{\partial^2\mathcal{J}}{\partial\eta^2}\right)\right],$$

$$\mathcal{L}^{(2)}(\hat{\mathbf{u}}) \equiv \frac{1}{\mathcal{J}^2}\frac{\partial^2\hat{\mathbf{u}}}{\partial\eta^2}, \quad \mathcal{L}^{(3)}(\hat{\mathbf{u}}) \equiv \frac{2}{\mathcal{J}^3}\begin{bmatrix} \frac{\partial u_\eta}{\partial\xi}\frac{\partial\mathcal{J}}{\partial\eta} - \frac{\partial u_\eta}{\partial\eta}\frac{\partial\mathcal{J}}{\partial\xi} \\ \\ \frac{\partial u_\xi}{\partial\eta}\frac{\partial\mathcal{J}}{\partial\xi} - \frac{\partial u_\xi}{\partial\xi}\frac{\partial\mathcal{J}}{\partial\eta} \end{bmatrix}. \tag{3.15}$$

The first equation in (3.12) is integrated forwards in time using the explicit Euler method, while Eqs. (3.14) are integrated using the implicit Crank–Nicolson method. Implicit treatment of $\mathcal{L}^{(3)}(\hat{\mathbf{u}})$ in the second sub-step of (3.14) requires iteratively updating the velocity. Now demanding that the third equation in (3.12) delivers a solenoidal velocity field at the end of a complete time step, we derive a Poisson equation for the projection function, $\hat{\nabla}^2\phi = (\rho/\Delta t)\hat{\nabla}\cdot\hat{\mathbf{u}}^*$, i.e.,

$$\frac{1}{\mathcal{J}^2}\left(\frac{\partial^2\phi}{\partial\xi^2} + \frac{\partial^2\phi}{\partial\eta^2}\right) = \frac{\rho}{\Delta t\,\mathcal{J}^2}\left(\frac{\partial(\mathcal{J}u_\xi^*)}{\partial\xi} + \frac{\partial(\mathcal{J}u_\eta^*)}{\partial\eta}\right), \tag{3.16}$$

where Δt is the time step and $\hat{\mathbf{u}}^*$ is the intermediate velocity at the end of the convection-diffusion step. The solution is found using standard Gauss–Seidel iteration, subject to the periodic condition in ξ and the homogeneous Neumann boundary conditions at $\eta = 0$ and $\eta = \eta_T$.

The periodicity boundary condition is imposed when solving the first sub-step in (3.14), and the no-penetration boundary condition at the walls is imposed when solving the second sub-step. To ensure the exact satisfaction of the no-slip condition at the end of the projection step, advancement over each time step is carried out in an iterative fashion by first introducing a wall slip condition for the intermediate velocity at the η convection-diffusion step. This intermediate slip value is gradually modified to annihilate the $O(\Delta t)$ wall slip introduced during the projection step. In practice, only a few iterations are necessary to reduce the numerical slip velocity down to a satisfactorily low level.

Once the velocity field has been updated over a time step, the interfacial marker points are advanced in the physical space with the interpolated velocity field using the explicit Euler method. To obtain the interpolated values of the velocity field at the interfacial nodes, the Cartesian velocity field is calculated, the grid nodes are mapped to the $\xi\eta$-plane using the approach described in Sect. 4.1, and the interpolation of the nodal velocity is carried out using the bicubic B-spline approximation in the $\xi\eta$-plane (e.g., [14]). The convection-diffusion equation (2.3) is simultaneously integrated by a finite-volume method [19]. In particular, following the advancement of the interfacial nodes, the surfactant concentration field is advanced in time using a semi-implicit method, where the geometrical properties of the interface are evaluated at the beginning of each time step. The typical values $\Delta t = 0.005\, d/U$ and $N_\xi = N_\eta = 64$ were used in the simulations.

3.3 Code validation

The performance of the numerical method was first assessed by considering pressure-driven flow of a single fluid in a channel, and comparing the numerical results with those obtained using a pseudospectral method [20]. The upper wall is flat, and the lower wall is described by the sinusoidal function $y_w = a_w\cos(kx)$, where a_w is the wave amplitude and $k = 2\pi/L$ is the wave number. In one test case, we set $a_w/d = 0.15$, $L/d = \pi/2$, and define the Reynolds number based on the bulk velocity,

$$\mathrm{Re}_{U_{\mathrm{bulk}}} \equiv \frac{3}{4}\frac{\rho\, d\, U_{\mathrm{bulk}}}{\mu} = 200, \quad U_{\mathrm{bulk}} \equiv \frac{1}{L\,d}\int_0^L\int_{y_w}^d u_x\,\mathrm{d}y\,\mathrm{d}x. \tag{3.17}$$

The factor of 3/4 ensures that the Reynolds number is identical to that based on the centerline velocity in Hagen–Poiseuille flow. To compare the two simulations, Luo and Bewley's [20] code was first run with constant U_{bulk}

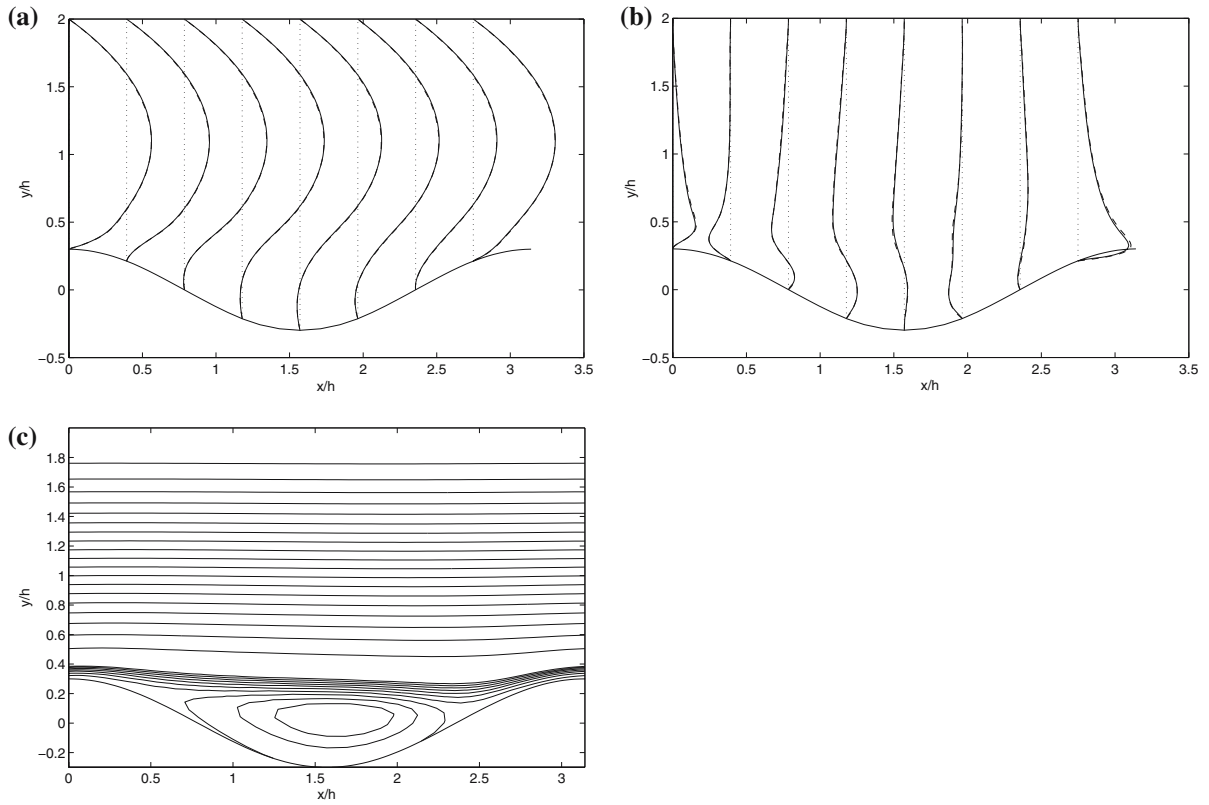

Fig. 2 Pressure-driven flow of a single fluid in a channel with a wavy lower wall. (**a**) Profiles of the x velocity component reduced by $3\,U_{\text{bulk}}$. (**b**) Profiles of the y velocity component reduced by $0.3\,U_{\text{bulk}}$. Profiles in (**a**) and (**b**) are plotted at locations $x/L = 0, 1/8, 2/8, \ldots, 7/8$. The present results are shown as solid lines, and the results of Luo and Bewley [20] are shown as dashed lines. (**c**) Streamline pattern

until a steady state was reached. A streamwise pressure drop that maintains the steady flow was then imposed in the present code to obtain the same steady bulk flow rate. Figures 2a, b show steady-state profiles of the Cartesian velocity components, u_x and u_y, at $x/L = 0, 1/8, 2/8, \ldots, 7/8$. The results of the present simulation, represented by the solid lines, are in excellent agreement with those of Luo and Bewley, shown as broken lines. Figure 2 shows that the u_x velocity has a nearly parabolic profile above the crests, and reverses direction inside the troughs. Near the lower wall, the u_y velocity reverses direction between $x/L = 1/8$ and $x/L = 2/8$, and then again at $x/L \simeq 6/8$, signaling the onset of flow separation. As the fluid enters through $x = 0$, the u_y velocity is positive, showing that the flow maintains a significant amount of upwards momentum due to inertia. Figure 2c shows the streamline pattern at steady state, confirming the aforementioned flow recirculation.

As a further application of the numerical method, we investigate the leveling of an interface over a sinusoidal wall under the action of surface tension in the absence of a mean flow, $U = 0$ and $\chi = 0$. The initial interfacial shape and surfactant concentration are described by

$$y(x, t = 0) = h_1 + \epsilon\, d\cos(kx), \qquad \Gamma(x, t = 0) = \Gamma_0\,[1 + \epsilon_\Gamma\,\cos(kx + \phi_\Gamma)]\,, \tag{3.18}$$

where ϵ and ϵ_Γ are dimensionless amplitudes, Γ_0 is the unperturbed surfactant concentration, and ϕ_Γ is the phase shift of the surfactant concentration wave with respect to the wall. The initial velocity field is zero in both fluids. Fig. 3 illustrates the evolution of the interface amplitude, a, plotted against the dimensionless time $\tau = t\gamma_0/(\mu_1 d)$ on a log-linear scale, for $L/d = \pi/2$, $h_1/d = 1/3$, $\lambda = 0.2$, $\epsilon = \epsilon_\Gamma = 0.1$ and $\phi_\Gamma = 0$. In these graphs, the instantaneous amplitude has been reduced by the initial amplitude, $a_0 \equiv \epsilon\, d$. Results are presented for Reynolds number $\text{Re} \equiv \rho\gamma d/\mu_1^2 = 40$ and 200, $a_w/d = 0$, 0.15, 0.25, and for both a clean and a surfactant–laden interface. The

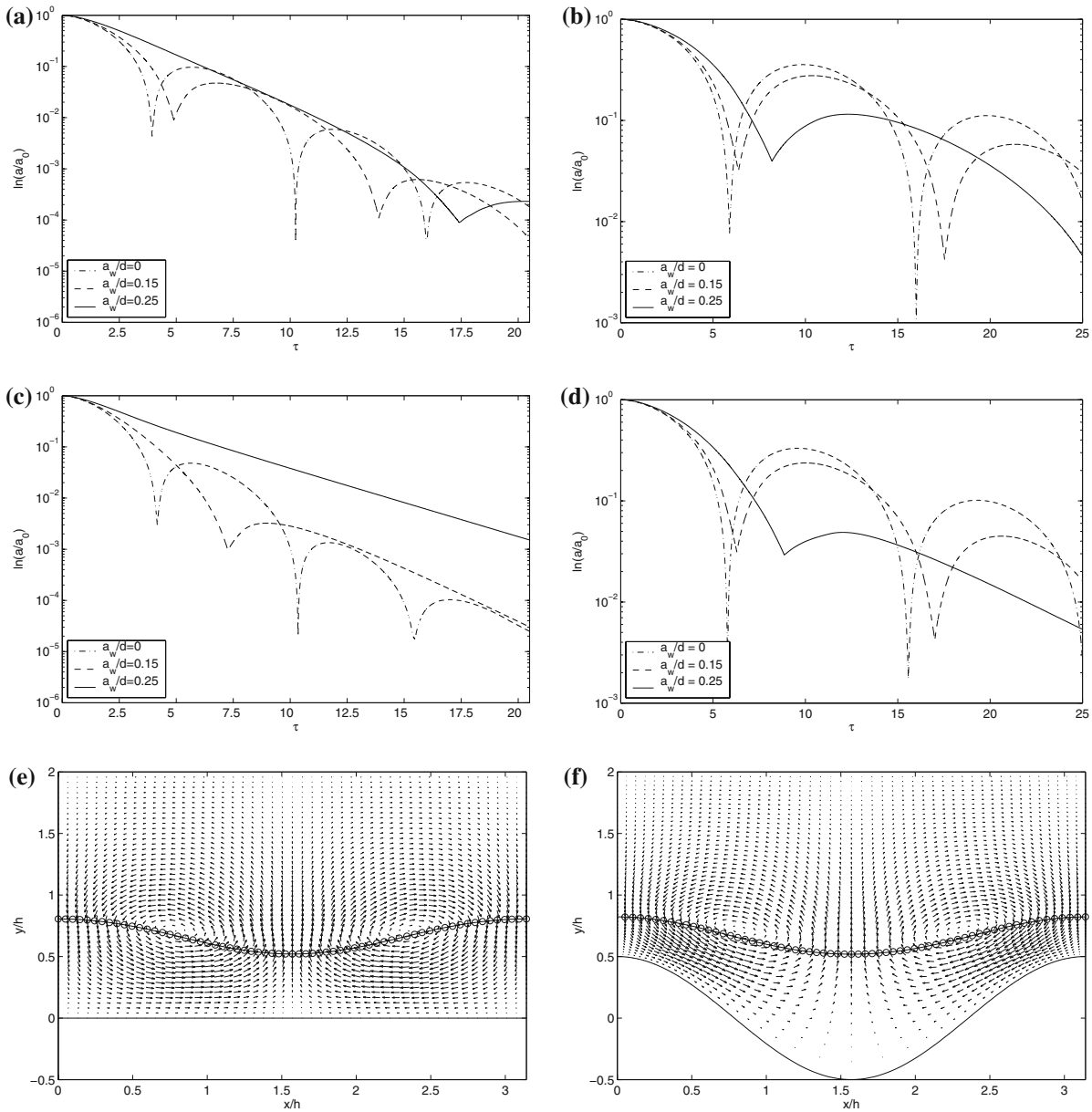

Fig. 3 Leveling of the interface between two otherwise quiescent fluids for several wall amplitudes, $L/d = \pi/2$, $h_1/d = 1/3$, $\lambda = 0.2$, and (**a**) Re $\equiv \rho\gamma d/\mu_1^2 = 40$, Ma $= 0$, (**b**) Re $= 200$, Ma $= 0$, (**c**) Re $= 40$, Ma $= 1$, $D_s = 0$, (**d**) Re $= 200$, Ma $= 1$, $D_s = 0$. (**e, f**) Velocity vector field and instantaneous interfacial shape at $\tau = 2.5$, for $L/d = \pi/2$, $h_1/d = 1/3$, $\lambda = 0.2$, Re $= 200$, Ma $= 0$, and $a_w/d = 0$ (**e**), 0.25 (**f**)

combined action of inertia and capillary effects causes the interface to overshoot and exhibit damped oscillations. In all cases, increasing the wall amplitude significantly increases the oscillation period and reduces the amplitude of the oscillation. Comparing the frames on the left- and right-hand side, we find that increasing the Reynolds number exacerbates the oscillations and delays the leveling of the interface. In the case of large wall amplitude, $a_w/d = 0.25$, increasing the Reynolds number also significantly reduces the period of the oscillation. Comparing the upper panels with the lower panels, we find that the surfactant has a significant influence on the dynamics of the motion, especially at the large wall amplitude. For the case shown in Fig. 3c, the surfactant prevents oscillations and

allows the interface to monotonically relax to the flat shape. Fig. 3e, f illustrates the instantaneous velocity vector fields for Re = 200, Ma = 0, and for $a_w/d = 0$ and $a_w/d = 0.25$, at time $\tau = 2.5$. Viscous eddies associated with the leveling action can be clearly identified.

3.4 Results and discussion

Next, we consider the two-layer channel flow and compare the results of the numerical simulations with the predictions of the linear perturbation analysis presented in the Appendix for a sinusoidal wall with amplitude $a_w/d = 0.025$. The numerical simulations were conducted on a 48×48 grid with an initial number of 64 interfacial marker points, taking the unperturbed unidirectional velocity field as an initial condition. Table 1 shows the amplitude and phase shift of the interfacial wave and the surfactant concentration wave for shear-driven flow with $L/d = \pi/2$, $h_1/d = 0.5$, $\mathrm{Re}_S \equiv \rho U d/\mu_1 = 20$, $\mathrm{Ca}_S \equiv \mu_1 U/\gamma_0 = 0.1$, $D_s = 0$, $\lambda = 1$ or 2, and Ma = 0 or 1. In all cases, the amplitude and phase shift of the interface obtained by the numerical simulations are in good agreement with the predictions of linear analysis. On the other hand, the numerical simulations somewhat overestimate the amplitude of the surfactant concentration wave, while faithfully reproducing the values for the phase shift.

Figure 4 shows steady interfacial profiles for $L/d = \pi/2$, $h_1/d = 0.15$, $\mathrm{Re}_S = 100$, $\mathrm{Ca}_S = 1$, and Ma = 0, and a sequence of increasing wall amplitudes, $a_w/d = 0.025$, 0.075, and 0.125. As expected, the difference between the numerical simulations and the linear analysis represented by the dashed lines is more pronounced for the highest wall amplitudes, $a_w/d = 0.125$. In all cases, the linear analysis underestimates the amplitude of the interface. Note that, in the case of Stokes flow, the linear analysis overestimates the amplitude of the interface [8]. Moreover, the theoretical prediction underestimates the phase shift of the interface when $\lambda = 1$ and overestimates it when $\lambda = 0.2$.

Figure 5 shows steady interfacial profiles for $L/d = \pi/2, h_1/d = 1/3, \lambda = 1.0, \mathrm{Ca}_S = 4, \mathrm{Ma} = 0, a_w/d = 0.15$, and several Reynolds numbers. The Stokes flow profile shown as a broken line was calculated using the boundary-element method of Luo and Pozrikidis [8]. The profile for $\mathrm{Re}_S = 4$ closely resembles that for Stokes flow, whereas the profile for $\mathrm{Re}_S = 20$ is slightly shifted downstream. As the Reynolds number is raised, the interface amplitude is reduced, the interfacial profile becomes more steep, and the valleys are shifted downstream.

Figure 6 illustrates the evolution of the interface for $\mathrm{Re}_S = 4$ and $\mathrm{Re}_S = 240$ from the initial flat configuration to a nearly steady state. In both cases, the interface quickly evolves into a traveling wave. For $\mathrm{Re}_S = 4$, a valley first develops above the descending part of the wall. As the interfacial wave is convected toward the ascending part of the wall, the trough is lifted upwards and then disappears as it reaches the wall crest. Eventually, the interface settles to a nearly sinusoidal shape. When $\mathrm{Re}_S = 240$, the wave steepens as it travels over a furrow in the wall, and it is smoothed as the wall starts to ascend. At later times, the amplitude of the interface is noticeably diminished. The weakened wave is unable to surmount a protrusion in the wall and, ultimately, it settles into the steady state

Table 1 Amplitude and phase-shift of the interfacial and the surfactant concentration waves for shear-driven flow with $L/d = \pi/2$, $h_1/d = 0.5$, $\mathrm{Re}_S = 20$, $\mathrm{Ca}_S = 0.1$, and $D_s = 0$

		Interfacial wave		Surfactant concentration wave	
		Amplitude $\lvert A\rvert$	Phase shift $\arg(A)$	Amplitude $\lvert\Gamma_1/\Gamma_0\rvert$	Phase shift $\arg(\Gamma_1)$
$\lambda = 1$, Ma = 0	Linear theory	0.057492	0.435173π	–	–
	Simulation	0.0594	0.4275π	–	–
$\lambda = 1$, Ma = 1	Linear theory	0.053505	0.402724π	0.044823	-0.481782π
	Simulation	0.0539	0.3957π	0.0526	-0.4711π
$\lambda = 2$, Ma = 0	Linear theory	0.071055	0.309061π	–	–
	Simulation	0.0757	0.2875π	–	–
$\lambda = 2$, Ma = 1	Linear theory	0.062859	0.298538π	0.069378	-0.549089π
	Simulation	0.0668	0.2875π	0.0847	-0.5602π

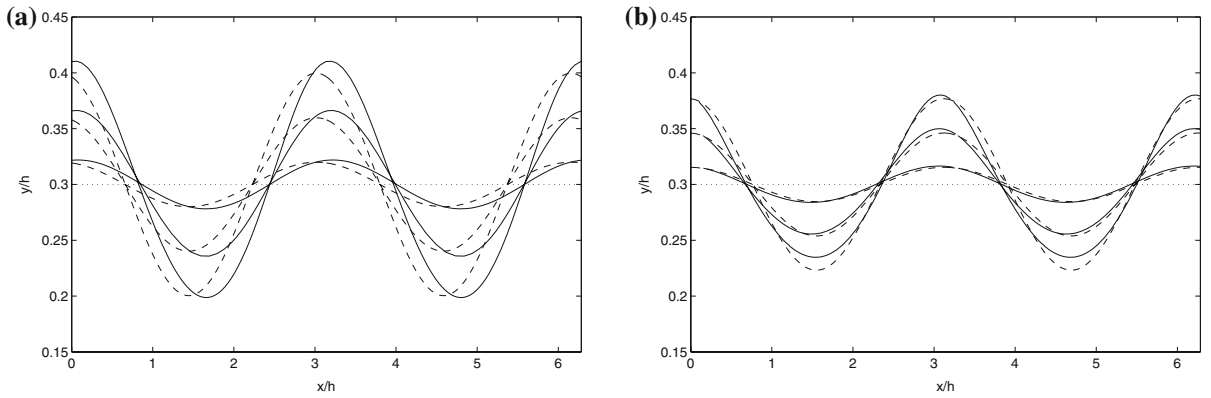

Fig. 4 Steady interfacial profiles for shear-driven flow over a sinusoidal wall with $L/d = \pi/2$, $h_1/d = 0.15$, $\lambda = 0.2$, $\mathrm{Re}_S = 100$, $\mathrm{Ca}_S = 1$, $\mathrm{Ma} = 0$, wall amplitude $a_w/d = 0.025$, 0.075, and 0.125, and (**a**) $\lambda = 1$, (**b**) $\lambda = 0.2$. The predictions of linear theory are shown as dashed lines

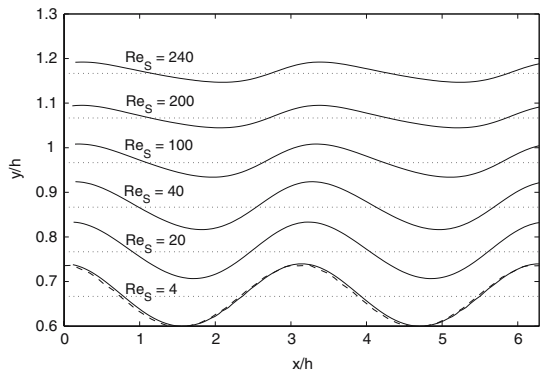

Fig. 5 Steady interfacial profiles for shear-driven flow over a sinusoidal wall with $L/d = \pi/2$, $h_1/d = 1/3$, $\lambda = 1.0$, $\mathrm{Ca}_S = 4$, $\mathrm{Ma} = 0$, and $a_w/d = 0.15$. The dashed line represents results for Stokes flow computed using a boundary-element method. For clarity, the profiles for different Reynolds numbers have been shifted in the y direction such that the mean locations (shown as dotted lines) are separated by the distance $0.1h$

shown in Fig. 5. Introducing surfactant delays the approach to the steady state, but does not significantly alter the ultimate profile attained.

Increasing either the Reynolds number or the wall amplitude much beyond the values shown in Fig. 5 leads to flow instability. In Fig. 7, we illustrate the evolution for $\mathrm{Re}_S = 100$, but with the wall amplitude increased to $a_w/d = 0.25$. The streamline patterns and interfacial profiles are shown as a sequence of instantaneous snapshots. The simulation is initiated at $\tau = 0$ with a flat interface. In this case, eddies formed within the wall furrows shift and deform slightly as the motion progresses, and the interface rapidly develops a sharp, localized front, which begins to overturn. The overturning is accelerated when the wave passes over a crest on the wall. As the wave contorts, the interfacial profile suggests that droplets are formed and begin to pinch off. The numerical method finally breaks down when the curvature of the interface becomes large enough. We have confirmed that increasing the grid resolution and reducing the time step do not make a significant difference to the results. Increasing the surface tension suppresses the instability and enables the flow to reach a steady state. This is demonstrated in Fig. 8 for the same parameter values as before, but with the lower capillary number $\mathrm{Ca}_S = 1$. The interface starts from a flat profile and reaches a steady state at about $\tau = 15$. The figure displays the steady state interface shape and streamlines of the flow at time $\tau = 25$.

As a final topic, we consider shear-driven flow over a wall comprised of a periodic sequence of semi-circular protrusions. An example is shown in Fig. 9 for $L/d = \pi/2$, $\lambda = 1$, $\mathrm{Ca}_S = 1$, $\mathrm{Re}_S = 100$, and $\mathrm{Ma} = 0$, and

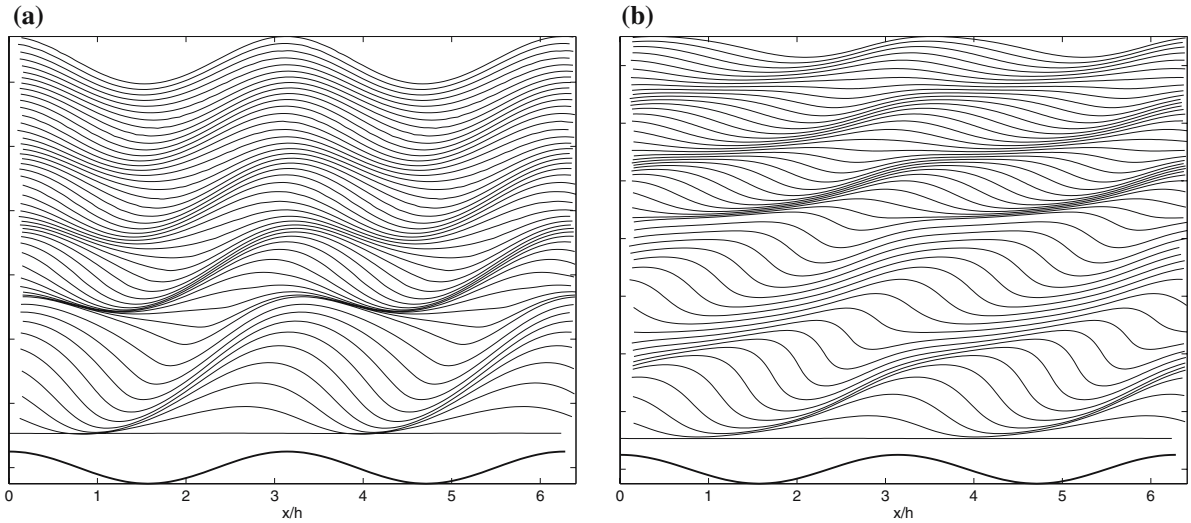

Fig. 6 Evolution of the interface for (**a**) $\mathrm{Re}_S = 4$ and (**b**) $\mathrm{Re}_S = 240$ from $\tau = 0$ (flat lines) to $\tau = 6.125$, with equal time intervals in between. The wall profile is shown as a thick line and with a reduced amplitude

for semi-circular protrusions of radius $L/4$. To accurately reflect the wall geometry in the conformal mapping, we take $N_b = 100$, $N_p = 400$ in computing the coefficients b_n in the coordinate transformation (3.2). Figure 9a displays interface profile and streamlines at steady state for $h_1/d = 0.45$, where the film thickness, h_1, is measured from the flat part of the wall to the mean location of the interface. Large eddies are apparent between adjacent protrusions. Figure 9b shows steady interfacial profiles for both $h_1/d = 0.45$ and $h_1/d = 0.5$. The solid lines represent the present results for $\mathrm{Re}_S = 100$, and the broken lines represent the results for Stokes flow computed by Luo and Pozrikidis [8]. Comparing the two sets of results, we find that inertia reduces the magnitude of the interfacial deformation and stretches the downstream side of the interface profile.

4 Discussion

We have studied the effect of inertia on two-layer flow over a corrugated wall when the interface between the fluids is contaminated with an insoluble surfactant.

In the Appendix, we used a perturbation approach to calculate the interfacial deformation when the amplitude of the wall undulations is small, and derived a linearized disturbance equation and boundary conditions for the perturbed flow valid at arbitrary Reynolds number. These were solved numerically using a Chebyshev tau method. The amplitude of the interfacial deformation and phase shift with respect to the wall was computed for a broad range of parameter values.

The Stokes flow calculations performed by Luo and Pozrikidis [8] demonstrated that the effect of the surfactant depends on the viscosity ratio, the distance of the interface from the lower wall, the capillary number, and the wave length of the corrugations. When the interface is close to the lower wall, surfactant increases the deformation experienced by the interface and induces a positive phase shift. As the interface approaches the upper wall, the phase shift vanishes. At non-zero Reynolds number, the phase shift does not tend to zero as the thickness of the lower layer is increased. For pressure-driven flow in particular, the phase shift varies rapidly as the upper wall is approached. For intermediate lower layer thicknesses, inertia has a strong influence on the phase shift, and may cause it to switch sign.

Irrespective of the lower layer thickness, raising the Reynolds number has little effect on the amplitude of the interfacial wave when the wave length of the wall corrugations is comparable to the channel width. The effect of

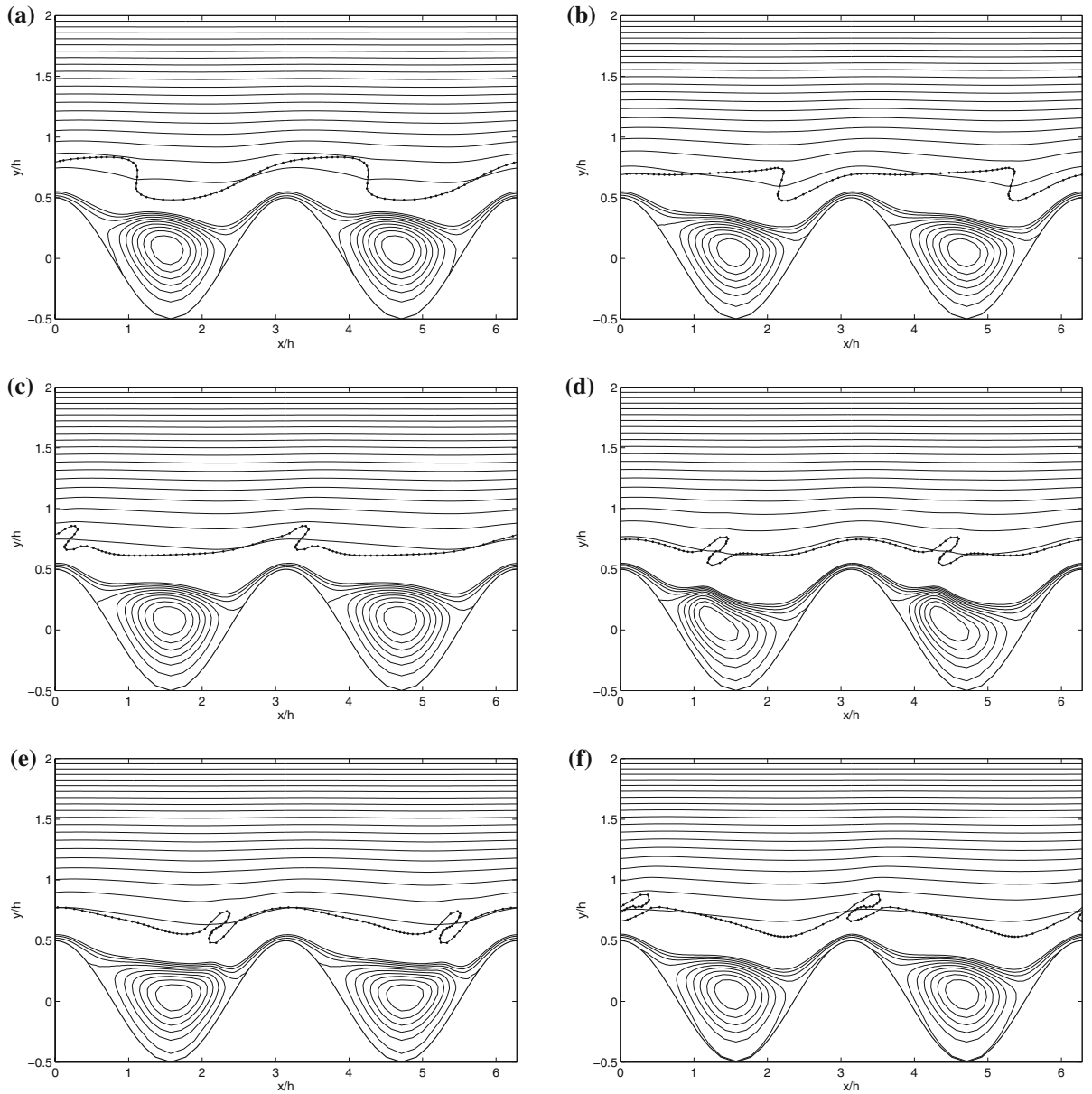

Fig. 7 Instantaneous streamline pattern and shape of the interface (shown as marked lines) for $L/d = \pi/2$, $h_1/d = 1/3$, $\lambda = 1$, $\mathrm{Ca}_S = 4$, $\mathrm{Re}_S = 100$, Ma $= 0$, $a_w/d = 0.25$ at times (**a**) $\tau = 0.625$, (**b**) $\tau = 1.25$, (**c**) $\tau = 1.875$, (**d**) $\tau = 2.5$, (**e**) $\tau = 3.125$, and (**f**) $\tau = 3.75$

inertia is more pronounced when the wave length of the corrugations is increased. In the context of shear-driven flow over a thin film coating a rough wall, we have found that increasing the Reynolds number reduces the interfacial disturbance for long-wave wall corrugations. For short-wave corrugations, the interfacial deformation is only slight, but is heightened by an increase in inertia. For either pressure-driven or shear-driven flow, elevating the surfactant concentration exaggerates the interfacial deformation up to an asymptotic limit. Similarly, raising the viscosity contrast between the layers leads to a larger interface amplitude. As the viscosity ratio is increased, the amplitude of the interface again approaches an asymptotic limit. Within the asymptotic regime, raising the Reynolds number for pressure-driven flow amplifies the interface deformation. The reverse picture applies for shear-driven flow when an increase in inertia leads to a decrease in the interfacial deformation.

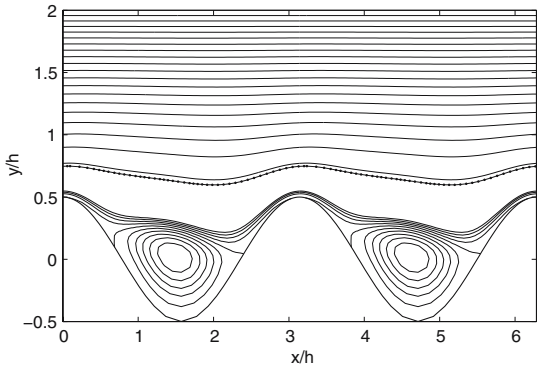

Fig. 8 The streamline pattern and steady interfacial profile (marked line) at time $\tau = 25$ for shear-driven flow with conditions $L/d = \pi/2$, $h_1/d = 1/3$, $\lambda = 1$, $\mathrm{Ca}_S = 1$, $\mathrm{Re}_S = 100$, $\mathrm{Ma} = 0$, and $a_w/d = 0.25$

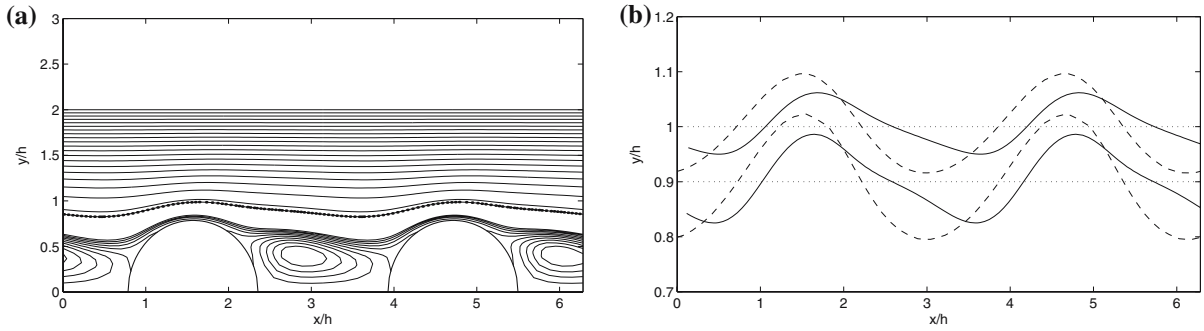

Fig. 9 Shear-driven flow over a corrugated wall with semi-circular protrusions of radius $L/4$ for $L/d = \pi/2$, $\lambda = 1$, $\mathrm{Ca}_S = 1$, $\mathrm{Re}_S = 100$, $\mathrm{Ma} = 0$. (**a**) The wall and interface (marked line) for $h_1/d = 0.45$. (**b**) The interfaces for $h_1/d = 0.45$ (lower solid line) and $h_1/d = 0.5$ (upper solid line). Corresponding results for Stokes flow are shown as dashed lines in (**b**)

An immersed interface method was used to carry out numerical simulations of two-layer flow at arbitrary Reynolds number. The results were validated by successful comparison first with the simulations for homogeneous fluid flow performed by Luo and Bewley [20], and second with the predictions of the linearized analysis. In the absence of a mean flow, a deformed interface settles under the influence of capillary forces to a flat resting configuration, while executing standing-wave oscillations whose period is an increasing function of the wall amplitude. Introducing surfactant may completely eliminate the oscillations, allowing the interface to relax monotonically to the flat resting state.

For shear-driven flow over a viscous film, we found that, when the wall corrugations are large, a clean interface attains a steady state profile whose phase shift with respect to the wall increases with Reynolds number. At the same time, the interfacial amplitude decreases as the Reynolds number is raised. Moreover, the steady interface tends to deviate from the sinusoidal shape found at lower Reynolds numbers. The character of the flow on the approach to the steady state changes markedly with the Reynolds number. In particular, wave steepening in the early stages of the flow development becomes more severe as the Reynolds number increases. At higher Reynolds number, or when the amplitude of the wall corrugations is sufficiently large, interfacial instability sets in. The interface develops localized contortions which become intensified every time the wave passes over a crest in the wall. Ultimately, the wave profiles overturn and begin to pinch together releasing droplets of the lower fluid.

Finally, we have described shear-driven flow over a sequence of semi-circular protrusions of arbitrary amplitude. As expected, large eddies develop between the protrusions. Inertia reduces the amplitude of the interfacial deformation and elongates the downstream side of the interfacial wave.

This study has concentrated on steady state solutions. We have found that surfactant promotes interfacial deformation, while inertia may ameliorate or exaggerate it, depending on parameter values. By following the evolution of a flat interface from an initial condition, the numerical simulations provide evidence that the steady solutions we

have computed are stable. We have also presented an example where the flow becomes unstable and the interface overturns. A complete study of the interfacial stability remains a subject for future investigation.

Acknowledgements This research was supported by a grant provided by the National Science Foundation. MGB was supported by the Nuffield Foundation under grant NUF-NAL-04.

Appendix A: Small sinusoidal undulations

In this appendix, we discuss steady interfacial shapes established when the amplitude of the lower wall is small compared to the channel width. To carry out this analysis, it is convenient to shift the x-axis so that the undisturbed interface for unidirectional flow through a channel with two plane walls is located at $y = 0$. The streamwise velocity profile of this base flow is given by

$$u_j^{(0)} = -\frac{\chi}{2\mu_j}\, y^2 + \xi_j y + u_I, \qquad v_j^{(0)} = 0, \tag{A.1}$$

for $j = 1, 2$. The interfacial velocity, u_I, is given by

$$u_I = \frac{\lambda}{\lambda + r} U + \frac{h^2 \chi}{\mu_1} \frac{2r}{(1+r)(\lambda + r)}, \tag{A.2}$$

where $h = (h_1 + h_2)/2$ is the semi-channel width and h_1, h_2 are the undisturbed thicknesses of the two layers. The interfacial shear rates appearing in (A.1) are given by

$$\xi_1 = \frac{U}{h_1} \frac{\lambda}{\lambda + r} - \frac{h\chi}{\mu_1} \frac{\lambda - r^2}{(1+r)(\lambda + r)}, \tag{A.3}$$

and $\xi_2 = \xi_1/\lambda$. The corresponding pressure field is given by

$$p_j^{(0)}(x, y) = -\chi\, x + P_0, \tag{A.4}$$

where P_0 is an inconsequential constant.

A.1 Linear perturbation analysis

In the presence of small undulations, the lower wall profile is described by the real part of

$$y_w(x) = -h_1 + \epsilon h_1\, \mathrm{e}^{\mathrm{i}kx}, \tag{A.5}$$

where $k = 2\pi/L$ is the wave number and ϵ is a small dimensionless parameter. Correspondingly, the interface is described by

$$y_I(x) = \epsilon \eta(x) = \epsilon h_1 A \mathrm{e}^{\mathrm{i}kx}, \tag{A.6}$$

where A is a complex constant. The perturbation of the surfactant concentration and surface tension are described by the analogous expansions,

$$\Gamma(x) = \Gamma_0 + \epsilon \Gamma_1\, \mathrm{e}^{\mathrm{i}kx}, \quad \gamma(x) = \gamma_0 + \epsilon \gamma_1\, \mathrm{e}^{\mathrm{i}kx}, \tag{A.7}$$

where γ_0 and Γ_0 are the undisturbed values, and γ_1, Γ_1 are dimensional complex constants to be determined as part of the solution. Substituting (A.7) in the equation of state (2.4), we obtain

$$\gamma_1 = -\mathrm{Ma}\, \frac{\gamma_0}{\Gamma_0}\, \Gamma_1, \tag{A.8}$$

where the Marangoni number Ma was defined in (2.5). The perturbation velocity, stream function, ψ, and pressure are written as

$$(u_j,\ v_j,\ \psi_j,\ p_j) = \left(u_j^{(0)},\ v_j^{(0)},\ \psi_j^{(0)},\ p_j^{(0)}\right) + \epsilon\left(u_j^{(1)},\ v_j^{(1)},\ \psi_j^{(1)},\ p_j^{(1)}\right) \tag{A.9}$$

for $j = 1, 2$, where the stream function is defined by $u_j = \partial\psi_j/\partial y$, $v_j = -\partial\psi_j/\partial x$. Substituting these expressions in the Navier–Stokes equation, eliminating the pressure, and writing $\psi_j^{(1)}(x, y) = \phi_j(y)\, \mathrm{e}^{\mathrm{i}kx}$, we obtain the disturbance equation

$$\phi_j'''' - 2k^2\phi_j'' + k^4\phi_j = \frac{\rho \mathrm{i}k}{\mu_j}\left[u_j^{(0)}(\phi_j'' - k^2\phi_j) - \frac{\mathrm{d}^2u_j^{(0)}}{\mathrm{d}y^2}\,\phi_j\right], \tag{A.10}$$

where a prime denotes a derivative with respect to y.

At the lower wavy wall, the no-penetration and no-slip conditions require

$$\phi_1 = 0, \qquad \phi_1' = -a_w\, h_1\, s \tag{A.11}$$

at $y = -h_1$, where the lower-wall shear rate, s, is given by

$$s = \frac{\mathrm{d}u_1^{(0)}}{\mathrm{d}y}\bigg|_{y=-h_1} = \frac{\chi}{\mu_1}h_1 + \xi_1. \tag{A.12}$$

Similar conditions apply at the upper wall,

$$\phi_2 = \phi_2' = 0 \tag{A.13}$$

at $y = h_2$. Continuity of velocity at the interface requires

$$\phi_1 = \phi_2, \qquad \phi_1' - \phi_2' = \frac{A}{\lambda}(1-\lambda)\xi_1 \tag{A.14}$$

at $y = 0$. The tangential component of the dynamic stress condition (2.2) requires

$$\left[\mu_j(\phi_j'' + k^2\phi_j + m_j A)\right]_2^1 = \frac{\mathrm{i}k\gamma_0}{u_I - \mathrm{i}kD_s}\,\mathrm{Ma}\,(\phi_1' + A\xi_1), \tag{A.15}$$

at $y = 0$, where $m_j = \mathrm{d}^2u_j^{(0)}/\mathrm{d}y^2 = -\chi/\mu_j$, and the normal component requires

$$\left[2\mu_j k^2\phi_j' - \mu_j(\phi_j''' - k^2\phi_j')\right]_2^1 = -\mathrm{i}k^3\gamma_0 A. \tag{A.16}$$

In both cases, the notation $[\bullet]_2^1$ denotes the jump $[\bullet]^1 - [\bullet]^2$. Note that the right-hand side of (A.15) has been derived by eliminating γ_1 using (A.8) and the linearized form of the surfactant transport equation (2.3). The latter yields the relation $(\phi_1' + A\xi_1)\,\Gamma_0 = (\mathrm{i}kD_s - u_I)\,\Gamma_1$ at $y = 0$ (e.g., [21]). Kinematic compatibility requires $D[y - \epsilon\eta(x)]/Dt = 0$ evaluated at the interface, where D/Dt is the material derivative, yielding

$$\phi_1 = -u_I A, \tag{A.17}$$

at $y = 0$. The task now is to solve (A.10) subject to conditions (A.11)–(A.17).

The solution was found numerically using a Chebyshev tau method (e.g., [22,23]). To implement the method, each fluid region is mapped onto the canonical domain of definition for Chebyshev functions using the two new coordinates

$$y_1 = \frac{2}{h_1}\left(y + \frac{h_1}{2}\right) \quad \text{in fluid 1}, \qquad y_2 = \frac{2}{h_2}\left(y - \frac{h_2}{2}\right) \quad \text{in fluid 2} \tag{A.18}$$

so that both y_1 and y_2 are defined over the interval $[-1, 1]$. Next, the functions ϕ_j, for $j = 1, 2$, are expanded in a truncated series of Chebyshev polynomials, $T_k(y_j)$, by setting

$$\phi_j(y_j) = \sum_{k=0}^{N_j} a_{jk}\, T_k(y_j), \tag{A.19}$$

where a_{jk} are a priori unknown constant coefficients, and N_1, N_2 are specified levels of truncation for each layer. Substituting (A.19) in (A.10) for $j = 1, 2$, and projecting the resulting equations onto $T_m(y_j)$ for $m = 0, \ldots, N_j - 4$ under the Chebyshev inner product,

$$\langle T_m(x),\, f(x)\rangle \;=\; \int_{-1}^{1} \frac{1}{\sqrt{1-x^2}}\, T_m(x)\, f(x)\, \mathrm{d}x, \tag{A.20}$$

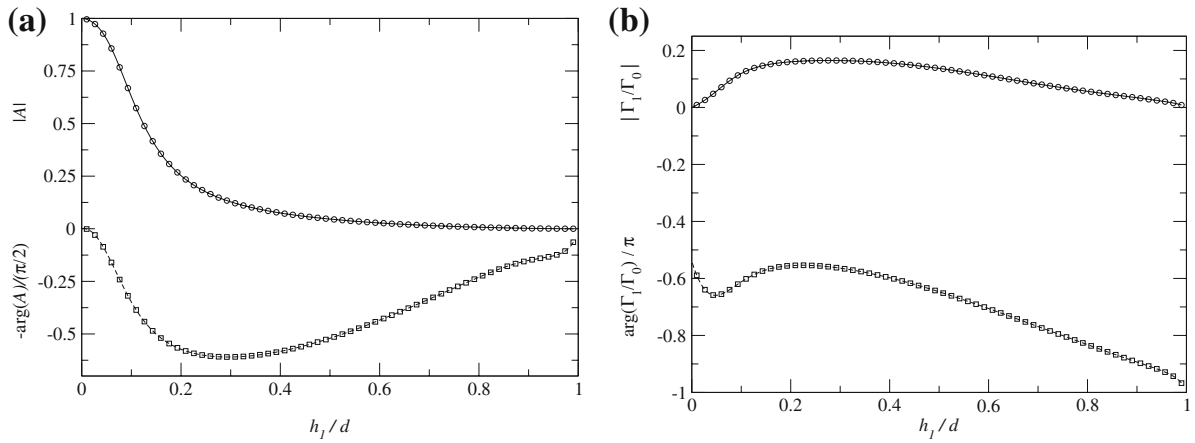

Fig. 10 Shear-driven Stokes flow in a channel with $L/d = 1$, $\lambda = 0.2$, $\mathrm{Ca}_S = 2.0$, $\mathrm{Ma} = 1.0$, $D_s = 0$. Magnitude (solid line) and phase shift (broken line) of (**a**) the interfacial amplitude A, and (**b**) perturbation in the surfactant concentration, Γ_1/Γ_0. In both cases, results computed using the Chebyshev tau method are shown as circles for the magnitude, and as squares for the phase shift

we derive a total of $N_1 + N_2 - 6$ algebraic equations. All integrals involving Chebyshev polynomials and their derivatives in the projection may be computed exactly using known identities and recursive relations (e.g., [22, pp. 159–161]. To complete the numerical problem, a set of eight more equations are derived by substituting (A.19) in the boundary conditions (A.11)–(A.17), yielding a complete set of $N_1 + N_2 + 2$ equations for the $N_1 + N_2 + 2$ coefficients a_{jk}, assembled in the linear system

$$\mathbf{A} \cdot \mathbf{X} = \mathbf{b}, \tag{A.21}$$

where $\mathbf{X} = (a_{10}, \ldots, a_{1N_1}, a_{20}, \ldots, a_{2N_2}, A)^T$. The solution is found by Gauss elimination. In practice, $N_1 = N_2 = 15$ is sufficient to produce accurate results for a wide range of parameter values. Results will be presented using these truncation levels, unless otherwise stated.

To test the numerical method, we set the right hand side of (A.10) equal to zero to obtain Stokes flow, and compare the results with those derived by Luo and Pozrikidis [8] using an analytical method. The amplitude and phase shift of the interfacial deformation and surfactant perturbation for shear-driven flow with $\lambda = 0.2$, $\mathrm{Ca}_S = 2$, $L/d = 1$, $\mathrm{Ma} = 1$ and $D_s = 0$ are shown in Fig. 10. The results of Luo and Pozrikidis [8] appear as solid and broken lines, and those computed using the Chebyshev tau method are shown as circles and squares. The excellent agreement validates the numerical method in the limit of Stokes flow.

A.2 Results and discussion

Figure 11a illustrates the effect of inertia on the interfacial amplitude for shear-driven flow with $L/d = 1$, $\lambda = 0.2$, $\mathrm{Ca}_S = 1.0$, $\mathrm{Ma} = 1.0$, $D_s = 0$, and Reynolds numbers Re_S in the range 0–100. Both Ca_S and Re_S are defined using the channel width as a length scale, $\mathcal{L} = d$. The results show that the interface amplitude, $|A|$, varies only weakly with the Reynolds number. When h_1/L is less than about 0.3, increasing the Reynolds number raises the interfacial amplitude; when h_1/L is larger than about 0.4, increasing the Reynolds number lowers the interfacial amplitude; a mixed behavior is observed for intermediate layer thicknesses. Figure 11b reveals that the fluid inertia has a strong influence on the interfacial phase shift, except for very thin lower layers. At sufficiently large Reynolds numbers, there is a value h_1/d where the phase shift is zero, which means that the interface is in phase with the lower wall. Luo and Pozrikidis [8] observed that, as the interface approaches the upper wall, $h_1/d \to 1$, the interfacial wave tends to become in-phase with the lower wall in Stokes flow. At non-zero Reynolds numbers, the phase shift remains finite in this limit. Figure 11c, d shows the effect of inertia on the amplitude and phase shift of the surfactant concentration wave. Figure 11c shows that inertia has only a minor effect on the amplitude of the concentration

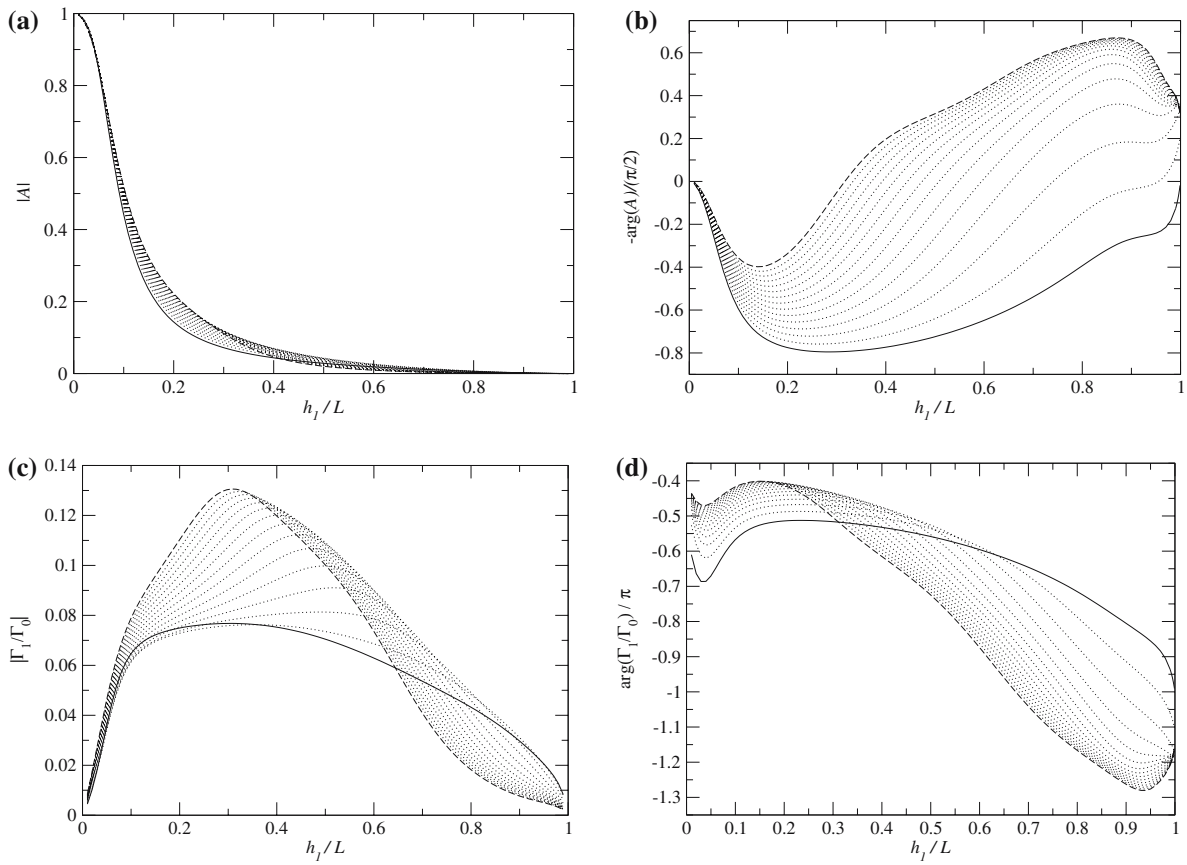

Fig. 11 Effect of the Reynolds number on (**a**) the interfacial amplitude, (**b**) the interfacial phase shift, (**c**) the surfactant amplitude, and (**d**) the surfactant phase shift, for shear-driven flow with $L/d = 1$, $\lambda = 0.2$, $\mathrm{Ca}_S = 1.0$, $\mathrm{Ma} = 1.0$, $D_s = 0$. The different curves correspond to Reynolds numbers that are evenly spaced from 0 (solid line) to 100 (broken line)

wave for thin lower-wall layers, and a pronounced effect for thicker layers. For smaller layer thicknesses, h_1/L, raising the Reynolds number increases the amplitude of the concentration wave, whereas, for large layer thicknesses, raising the Reynolds number decreases the amplitude of the surfactant concentration wave. For intermediate layer thicknesses, an increase or decrease may occur. A similar reversal in the role of the Reynolds number is experienced by the phase shift, as illustrated in Fig. 11d.

Results for pressure-driven flow are shown in Fig. 12 for $L/d = 1$, $\lambda = 0.2$, $\mathrm{Ca}_P = 1.0$, $\mathrm{Ma} = 1.0$, and Reynolds numbers, Re_P, in the range 0–100. Both Ca_P and Re_P are based on the length scale $\mathcal{L} = d$. As in the case of shear-driven flow, inertia has only a mild influence on the amplitude of the interface, $|A|$. However, in the case of pressure-driven flow, inertia has a significant influence on the interfacial phase shift even for thin lower layers. Moreover, as the interface approaches the upper wall, the interfacial phase shift changes rapidly and does not tend to zero, even for Stokes flow. As in the case of shear-driven flow, the effect of inertia on the amplitude and phase shift of the surfactant perturbation depends on the location of the unperturbed interface. For small values of h_1/L, raising the Reynolds number produces an increase in the perturbation amplitude. Conversely, for larger values of h_1/L, raising the Reynolds number reduces the amplitude of the surfactant perturbation.

The effect of the wave number of the wall corrugations, kh_1, is shown in Fig. 13 for $h_1/d = 0.1$, $\lambda = 0.2$, $\mathrm{Ma} = 1.0$, and $D_s = 0$. To isolate the effect of the wave length, the capillary and Reynolds numbers are now based on the lower layer thickness scale $\mathcal{L} = h_1$. In these computations, the Chebyshev truncation levels were set at the increased level $N_1 = N_2 = 30$. Fig. 13a illustrates the effect of kh_1, on the interfacial amplitude, $|A|$, for

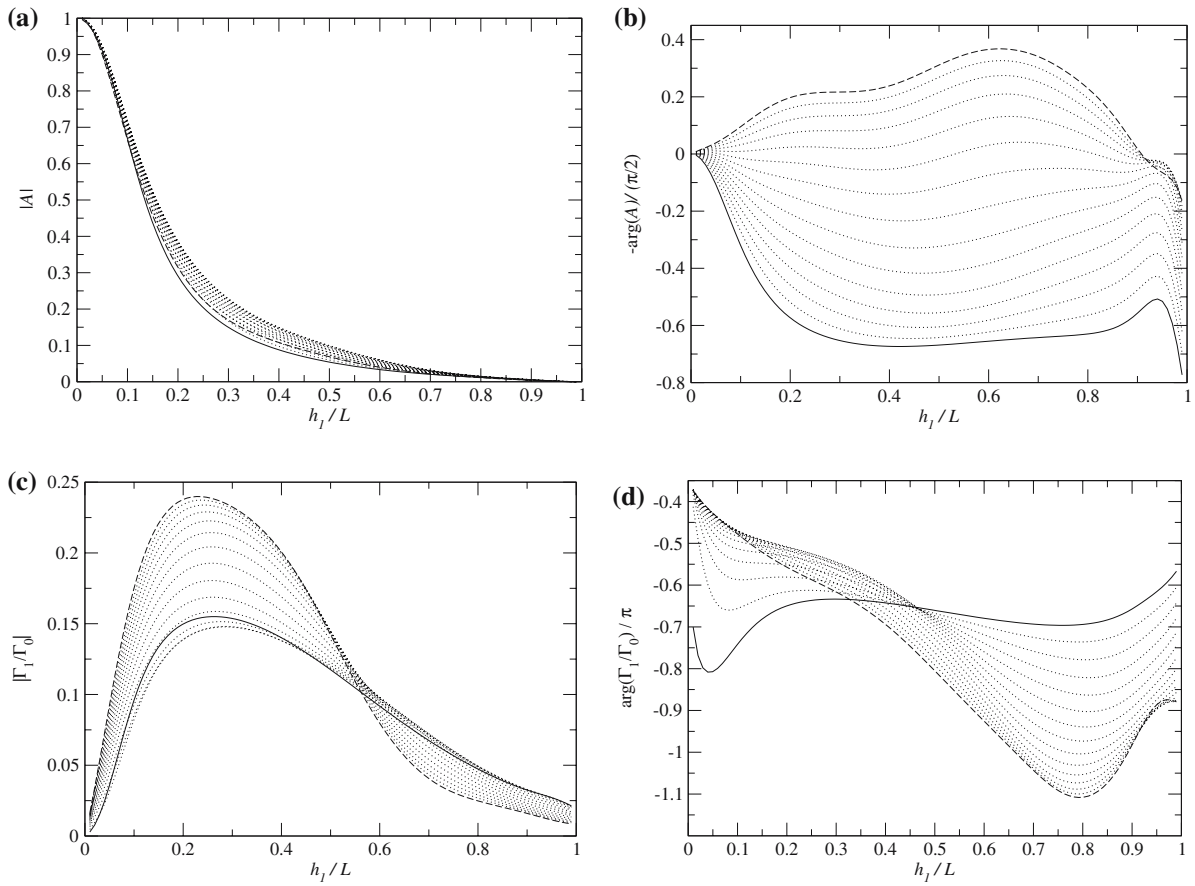

Fig. 12 Effect of Reynolds number on (**a**) the interfacial amplitude, (**b**) the interfacial phase shift, (**c**) the surfactant amplitude, and (**d**) the surfactant phase shift, for pressure-driven flow with $L/d = 1$, $\lambda = 0.2$, $\mathrm{Ca}_P = 1.0$, $\mathrm{Ma} = 1.0$, $D_s = 0$. The different curves correspond to Reynolds numbers that are evenly spaced from 0 (solid line) to 100 (broken line)

pressure-driven flow with $\mathrm{Ca}_P = 0.01$ and Reynolds numbers, Re_P, ranging from 0 to 1. The graphs show that, as the wave number kh_1 is raised, the perturbation amplitude decreases in a monotonic fashion. At high values of kh_1, the graphs for different Reynolds number intertwine. A similar behavior is observed for shear-driven flow, as illustrated in Fig. 13b for $\mathrm{Ca}_S = 1.0$. When kh_1 is small, raising the Reynolds number reduces the interfacial amplitude. On the other hand, for values of kh_1 above about 1.11, raising the Reynolds number promotes the interfacial deformation.

Figure 14 illustrates the effect of the Marangoni number for $kh_1 = \pi/5 \approx 0.63$, $h_1/d = 0.1$, $\lambda = 0.2$, and $D_s = 0$. The capillary and Reynolds numbers are based on the channel width, $\mathcal{L} = d$. In these calculations, the Chebyshev truncation levels were fixed at $N_1 = N_2 = 30$. Fig. 14a shows results for pressure-driven flow with $\mathrm{Ca}_P = 1.0$, and Fig. 14b shows results for shear-driven flow with $\mathrm{Ca}_S = 1.0$. For either pressure-driven or shear-driven flow, raising the Marangoni number increases the interfacial amplitude. Consequently, the surfactant has a stronger effect on the deformation of the interface.

Figure 15 shows the effect of the viscosity ratio λ for $L/d = 1$, $h_1/L = 0.2$, $\mathrm{Ma} = 1.0$, and $D_s = 0$. The capillary and Reynolds numbers are based on the channel width scale $\mathcal{L} = d$. Fig. 15a shows graphs of $|A|$ against λ for pressure-driven flow when $\mathrm{Ca}_P = 1.0$, and Fig. 15b shows results for shear-driven flow when $\mathrm{Ca}_S = 1.0$. In both cases, each curve corresponds to a different Reynolds number ranging from 0 to 50. As the viscosity ratio is raised from zero, the interface amplitude quickly rises before gradually decaying to an asymptotic limit corresponding to a very viscous upper fluid. Interestingly, in the case of pressure-driven flow, the curve for $\mathrm{Re}_P = 0$ rises with

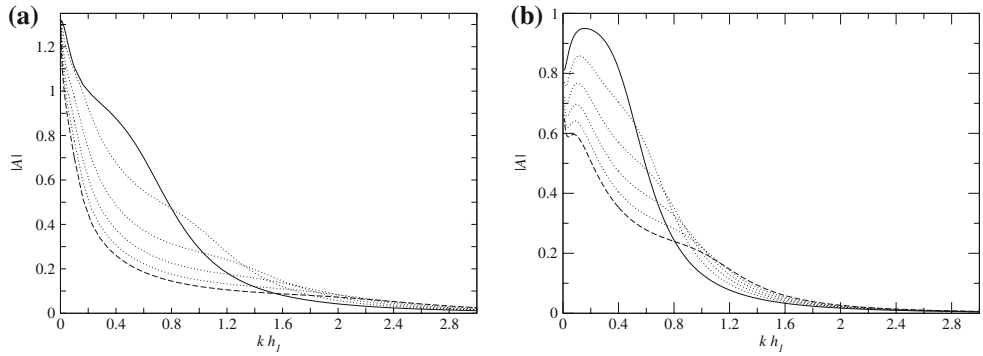

Fig. 13 Variation of the interface deformation amplitude, $|A|$, with the wave number, kh_1, for $h_1/d = 0.1$, $\lambda = 0.2$, Ma $= 1.0$ and $D_s = 0$. (**a**) Pressure-driven flow for $\mathrm{Ca}_P = 0.01$ and $\mathrm{Re}_P = 0$ (solid line) up to $\mathrm{Re}_P = 1$ (broken line) with equal intervals in between (dotted lines). (**b**) Shear-driven flow for $\mathrm{Ca}_S = 1.0$ and $\mathrm{Re}_S = 0$ (solid line) up to $\mathrm{Re}_S = 100$ (broken line) with equal intervals in between (dotted lines)

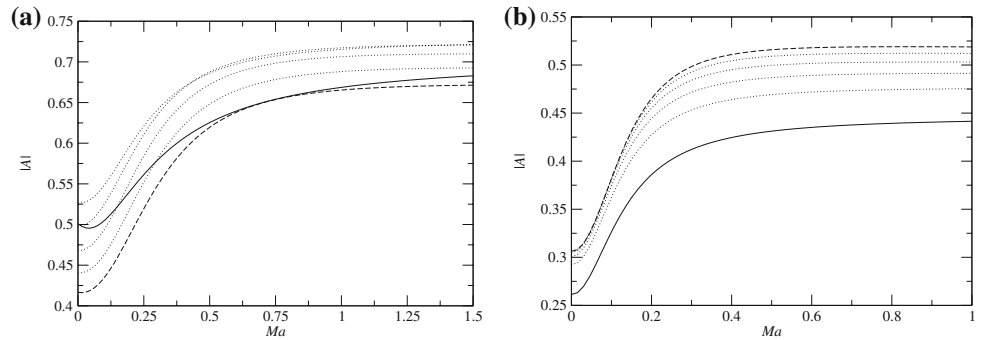

Fig. 14 Effect of the Marangoni number of the interface amplitude for $kh_1 = \pi/5 \approx 0.63$, $h_1/d = 0.1$, $\lambda = 0.2$, and $D_s = 0$. (**a**) Pressure-driven flow with $\mathrm{Ca}_P = 1.0$ and various Re_P, and (**b**) shear-driven flow with $\mathrm{Ca}_S = 1.0$ and various Re_S. In both cases, the Reynolds number varies from 0 (solid line) to 100 (broken line) with equal intervals in between (dotted lines)

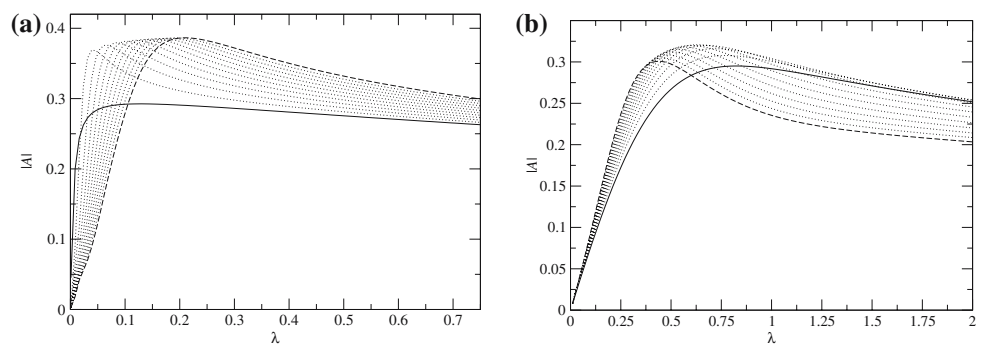

Fig. 15 Effect of the viscosity ratio on the interface amplitude for $L/d = 1$, $h_1/L = 0.2$, Ma $= 1.0$ and $D_s = 0$. (**a**) Pressure-driven flow for $\mathrm{Ca}_P = 1.0$ and $\mathrm{Re}_P = 0$ (solid line) up to $\mathrm{Re}_P = 50$ (broken line) with equal intervals in between (dotted lines). (**b**) Shear-driven flow for $\mathrm{Ca}_S = 1.0$ and $\mathrm{Re}_S = 0$ (solid line) up to $\mathrm{Re}_S = 50$ (broken line) with equal intervals in between (dotted lines)

the highest initial slope. When the viscosity ratio is high, inertia tends to increase the interfacial deformation. The situation is reversed for shear-driven flow where the Stokes flow curve exhibits the most gentle growth. For large viscosity ratios, increasing the Reynolds number reduces the amplitude of the interface.

References

1. Cabal A, Szumbarski J, Floryan JM (2002) Stability of flow in a wavy channel. J Fluid Mech 457: 191–212
2. Floryan JM (2005) Two-dimensional instability of flow in a rough channel. Phys Fluids 17(4):044101
3. Wang CY (1981) Liquid film flowing slowly down a wavy incline. AIChE J 27: 207–212
4. Kang F, Chen K (1995) Gravity-driven two-layer flow down a slightly wavy periodic incline at low Reynolds numbers. Int J Multiphase Flow 21: 501–513
5. Pozrikidis C (2003b) Effect of surfactants on film flow down a periodic wall. J Fluid Mech 496: 105–127
6. Vlachogiannis M, Bontozoglou V (2002) Experiments on laminar film flow along a periodic wall. J Fluid Mech 457: 133–156
7. Wierschem A, Scholle M, Aksel N (2003) Vortices in film flow over strongly undulated bottom profiles at low Reynolds numbers. Phys Fluids 15: 426–435
8. Luo H, Pozrikidis C (2006) Shear-driven and channel flow of a liquid film over a corrugated or indented wall. J Fluid Mech 556: 167–188
9. Li X, Pozrikidis C (1997) The effect of surfactants on drop deformation and on the rheology of dilute emulsions in Stokes flow. J Fluid Mech 341: 165–194
10. Pozrikidis C (2001) Interfacial dynamics for Stokes flow. J Comp Phys 169: 250–301
11. Adamson AW (1990) Physical chemistry of surfaces. Wiley, London
12. Pozrikidis C (2004) Instability of multi-layer channel and film flows. Adv Appl Mech 40: 179–239
13. Peskin CS (2002) The immersed boundary method. Acta Numerica 11: 479–517
14. Pozrikidis C (2004) Effect of inertia on the Marangoni instability of two-layer channel flow, Part I: numerical simulations. J Engng Math 50: 311–327
15. Blyth MG, Luo H, Pozrikidis C (2006) Stability of axisymmetric core-annular flow in the presence of an insoluble surfactant. J Fluid Mech 548:207–235
16. Caponi EA, Fornberg B, Knight DD, Mclean JW, Saffman PG, Yuen HC (1982) Calculations of laminar viscous flow over a moving wavy surface. J Fluid Mech 124: 347–362
17. Pozrikidis C (1997) Introduction to theoretical and computational fluid dynamics. Oxford University Press, New York
18. Pozrikidis C (2003) On the relationship between the pressure and the projection function for the numerical computation of incompressible flow. Euro J Mech B / Fluids 22: 105–121
19. Yon S, Pozrikidis C (1998) A finite-volume / boundary-element method for flow past interfaces in the presence of surfactants, with application to shear flow past a viscous drop. Computers and Fluids 27: 879–902
20. Luo H, Bewley TR (2004) On the contravariant form of the Navier–Stokes equation in time-dependent curvilinear coordinate systems. J Comp Phys 199(1): 355–375
21. Blyth MG, Pozrikidis C (2004) Evolution equations for the surface concentration of an insoluble surfactant; stability of an elongating thread and a stretched interface. Theor Comp Fluid Dyn 17(3): 147–164
22. Gottlieb D, Orszag SA (1977) Numerical analysis of spectral methods. SIAM, Philadelphia
23. Dongarra JJ, Straughan B, Walker DW (1996) Chebyshev tau-QZ algorithm methods for calculating spectra of hydrodynamic stability problems. Appl Num Math 22: 399–434